

Interstellar gas towards CTB 37A and the TeV gamma-ray source HESS J1714–385

Nigel I. Maxted^{1*}, Gavin P. Rowell¹, Bruce R. Dawson¹, Michael G. Burton², Yasuo Fukui³, Andrew Walsh⁴, Akiko Kawamura³, Hirotaka Horachi³, Hidetoshi Sano³, Satoshi Yoshiike³ & Tatsuya Fukuda³

¹*School of Chemistry & Physics, University of Adelaide, Adelaide, 5005, Australia*

²*School of Physics, University of New South Wales, Sydney, 2052, Australia*

³*School of Physics, Nagoya University, Furocho, Chikusa-ku, Nagoya, Aichi, 464-8602, Japan*

⁴*International Centre for Radio Astronomy Research, Curtin University, GPO Box U1987, Perth, Australia*

Accepted 2013 June 23. Received 2013 June 20; in original form 2012 October 26

ABSTRACT

Observations of dense molecular gas towards the supernova remnants CTB 37A (G348.5+0.1) and G348.5–0.0 were carried out using the Mopra and Nanten2 radio telescopes. We present CO(2-1) and CS(1-0) emission maps of a region encompassing the CTB 37A TeV gamma-ray emission, HESS J1714–385, revealing regions of dense gas within associated molecular clouds. Some gas displays good overlap with gamma-ray emission, consistent with hadronic gamma-ray emission scenarios. Masses of gas towards the HESS J1714–385 TeV gamma-ray emission region were estimated, and were of the order of 10^3 – $10^4 M_{\odot}$. In the case of a purely hadronic origin for the gamma ray emission, the cosmic ray flux enhancement is ~ 80 – 1100 times the local solar value. This enhancement factor and other considerations allow a discussion of the age of CTB 37A, which is consistent with $\sim 10^4$ yr.

Key words: molecular data - supernovae: individual: CTB 37A - ISM: clouds - cosmic rays - gamma rays: ISM.

1 INTRODUCTION

Gamma ray observations may be the key to solving one of the longest unsolved mysteries in astrophysics, the origin of cosmic rays (hereafter CRs). Since gamma-rays are byproducts of cosmic ray interactions, high gamma-ray fluxes are expected from regions with enhanced cosmic ray densities, such as near cosmic ray acceleration sites. The leading theory to explain the acceleration of these particles is first order Fermi acceleration in the shocks of supernova remnants (hereafter SNRs).

A candidate region for CR-acceleration is CTB 37, which is comprised of three SNRs: CTB 37A (G348.5+0.1), CTB 37B (G348.7+0.3) and G348.5–0.0. CTB 37A was initially discovered at radio wavelengths (Clark et al. 1975) and was recently observed to emit at TeV energies (HESS J1714–385, Aharonian et al., 2008a). GeV-energy excesses have also been detected (3EG J1714–3857, Green et al., 1999; Hartman et al., 1999, 1FGL J1714.5–3830, Castro & Slane, 2010).

The CTB 37A radio continuum emission (see Figure 1a) is suggestive of a ‘break-out’ morphology. Strong shell-shaped emission emanates from the eastern (galactic coordinate system) section and a weaker lobe or ‘break-away’ region extends in a western direction. Reynoso & Mangum (2000) observed CO(1-0) emission towards CTB 37A and investigated the possibility that the observed features are caused by constraining molecular gas along the north, east and south boundaries. They found associated $v_{\text{LSR}} \sim -65 \text{ km s}^{-1}$ molecular clouds around the northern and eastern edges of the CTB 37A radio continuum emission, while minimal gas was seen in the location of the ‘break-out’ features to the west. In the south however, inconsistent with predictions, no gas (as traced by CO(1-0)) was seen to be constraining the remnant.

Knowledge of gas distribution is also important when considering a hadronic (pion production via CR collisions with gas) origin for the CTB 37A gamma-ray emission, although the nature of the parent particle population (leptonic and/or hadronic) is not entirely clear. Non-thermal X-ray emission is absent from the CTB 37A radio rim (Frail et al. 1996), which, in the presence of strong magnetic fields would

* E-mail: nigel.maxted@adelaide.edu.au

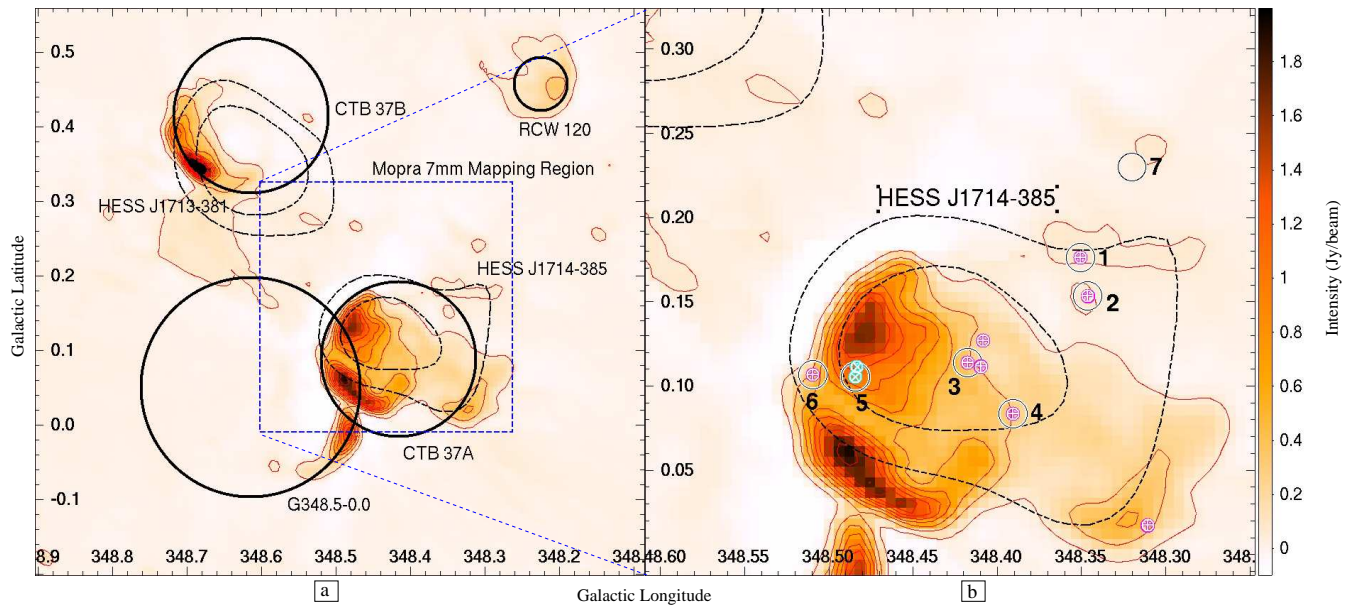


Figure 1. (a) Molonglo 843 MHz radio continuum image showing CTB 37 (Clark et al. 1975). 80 and 100 gamma-ray excess count contours of HESS J1714–385 (CTB 37A) and HESS J1713–381 (CTB 37B) (black, dashed) (Aharonian et al. 2008a) and Molonglo 843 MHz radio continuum (bandwidth ~ 4.4 MHz) contours (red) are overlaid. A dashed blue square represents the region observed with Mopra (this work) and large labeled black circles mark the approximate locations and extents of objects of interest, as visually approximated from the 843 MHz image. (b) Similar to (a), but zoomed on CTB 37A. Crosses represent both the ~ -65 km s⁻¹ (pink, +) and ~ -25 km s⁻¹ (cyan, x) OH maser populations (Frail et al. 1996), circles represent the position and beam FWHM of 7 mm Mopra deep ON-OFF switched pointings.

imply a lack of ongoing high energy electron acceleration. Indeed, Brogan et al. (2000) measured strong magnetic fields (0.22-1.5 mG) towards shocked regions of CTB 37A, and in such environments TeV leptons have limited lifetimes due to synchrotron losses (synchrotron lifetimes of $\lesssim 250$ yr, very short compared to the SNR age, see § 5.3). If the high energy lepton population is diminished towards the CTB 37A radio rim, which it appears to be, a hadronic scenario for gamma-ray emission production would be favourable (Aharonian et al. 2008a).

Alternatively, a leptonic scenario for CTB 37A is supported by the presence of a coincident region of non-thermal X-ray emission (Aharonian et al. 2008a). This could possibly indicate a pulsar wind nebulae (PWN) accelerating electrons within a blast wave (making CTB 37A a composite SNR), but this hypothesis is complicated by the non-detection of a point-like source or pulsar within the extended non-thermal emission (Aharonian et al. 2008a). Certainly, the non-thermal and thermal emission from the outer rim and centre of CTB 37A, respectively, indicate that CTB 37A is a mixed-morphology SNR. Results by Brandt et al. (2011) are suggestive of a significant Bremsstrahlung emission component between 1 and 100 GeV, with a hadronic component dominating at TeV energies and above, but the question of the nature of the emitting particle population is still largely an open question.

Also present towards the CTB 37A region (Aharonian et al. 2008a), are 1720 MHz OH masers, which are indicators of shock-gas interactions, likely triggered by SNR shocks (Aharonian et al. 2008a; Frail et al. 1996). However, the interpretation of this data is confused by the existence of a coincident partial shell SNR, G348.5–0.0

(Milne et al. 1979; Kassim et al. 1991), which can be seen in 843 MHz radio continuum emission in Figure 1a. Two masers comprise a population at line-of-sight-velocity, $v_{\text{LSR}} \sim -22$ km s⁻¹ while eight comprise a second population at $v_{\text{LSR}} \sim -65$ km s⁻¹. Although it has been suggested that the 2 maser populations may be attributable to each of the 2 SNRs separately, recent work by Tian & Leahy (2012) (hereafter TL2012) demonstrates that CTB 37A may simply be associated with multiple varied-velocity clouds. This suggests that both populations of masers may be attributable to CTB 37A (and neither would be associated with G348.5–0.0).

Reynoso & Mangum (2000) found molecular CO(1-0) cloud associations towards most of the masers, but two $v_{\text{LSR}} \sim -65$ km s⁻¹ OH masers (Locations 1 and 2, see Figure 1b) did not have clear CO emission counterparts at corresponding velocities and locations. The formation of 1720 MHz OH masers requires large gas densities of $n_{\text{H}_2} \sim 10^4$ - 10^5 cm⁻³ (Draine et al. 1983; Frail et al. 1998), but CO(1-0) emission has a critical density of $\lesssim 10^3$ cm⁻³ and quickly becomes optically thick. As Reynoso & Mangum (2000) suggest, to probe deeper, observations of dense gas tracers are required.

In addition to being conducive to OH maser generation, dense gas may significantly affect the dynamics of the SNR shock motion, while also providing denser targets for gamma-ray-producing hadronic cosmic ray interactions. Knowing the location of dense gas may lead to both an explanation for the ‘break-out’ morphology of the radio continuum emission and more detailed modeling of the CTB 37A TeV emission. Previous studies have noted that dense gas may hinder CR diffusion and change the resul-

tant high energy photon spectrum from hadronic interactions (Gabici et al. 2009; Casanova 2011; Fukui et al. 2012; Maxted et al. 2012).

To complement existing Nanten2 CO(2-1) and Southern Galactic Plane Survey (SGPS) HI data (McClure-Griffiths et al. 2005; Haverkorn et al. 2006; Tian & Leahy 2012) we took 7 mm observations of the CTB 37A region with the Mopra radio telescope. We targeted the gas tracer CS(1-0) (critical density $\sim 8 \times 10^4 \text{ cm}^{-3}$) to investigate dense gas and simultaneously searched for the potential shock-tracers SiO(1-0) and CH₃OH (motivated by results towards the SNR W28, Nicholas et al., 2012) to search for shocked gas related to SNR activity.

To investigate the gas distribution towards CTB 37A, we applied gas parameter calculation methods presented in §3 to several clouds of gas, which we consider separately in subsections of §4. In §5.1 we compare column densities estimated by us to estimates by previous authors. In §5.2 we use our gas mass estimates to estimate the cosmic ray density in several scenarios of gamma-ray emission from hadronic processes for CTB 37A. Finally, in §5.3, we discuss the age of CTB 37A.

1.1 Distance

By noting that towards CTB 37A, HI absorption occurs in gas at $v_{\text{LSR}} \sim -110 \text{ km s}^{-1}$, but not from gas that lies at $v_{\text{LSR}} \sim -65 \text{ km s}^{-1}$, Caswell et al. (1975) concluded that the $v_{\text{LSR}} \sim -110 \text{ km s}^{-1}$ gas was nearer to us than CTB 37A. Assuming that the line-of-sight-velocities were primarily due to galactic kinematic motions, the authors recognised that the $v_{\text{LSR}} \sim -65 \text{ km s}^{-1}$ gas must be on the ‘far-side’ (past the tangent point) of the galaxy in order to be spatially behind the $v_{\text{LSR}} \sim -110 \text{ km s}^{-1}$ gas. The distance of the CTB 37A radio emission was thus constrained to be between 6.7 and 13.7 kpc (assuming $l \sim 349^\circ$) (this kinematic distance constraint relied on a value of 10 kpc for the orbital radius of the sun with respect to the galactic centre).

More recent high-resolution SGPS data allowed TL2012 to not only find partial HI absorption at $v_{\text{LSR}} \sim -65 \text{ km s}^{-1}$, but also a distinct lack of HI absorption towards previously-overlooked gas at $v_{\text{LSR}} \sim -145 \text{ km s}^{-1}$, as traced by CO(1-0) (Reynoso & Mangum 2000). TL2012 suggest that since the $v_{\text{LSR}} \sim -65 \text{ km s}^{-1}$ gas lies between the $v_{\text{LSR}} \sim -110 \text{ km s}^{-1}$ (HI absorption) and $v_{\text{LSR}} \sim -145 \text{ km s}^{-1}$ (no HI absorption) gas, the $v_{\text{LSR}} \sim -65 \text{ km s}^{-1}$ gas may plausibly be in a non-circular orbit, as would be the case if CTB 37A is within the inner 3 kpc of the galaxy, influenced by the gravitational potential of the Perseus arm. This implies that the CTB 37A SNR distance may be between 6.3 and 9.5 kpc, thus we assume a distance of 7.9 ± 1.6 in our analyses. HI absorption information is summarised in Table 1.

2 OBSERVATIONS

In April of 2010, we observed and co-added 5 Mopra OTF (on the fly) $19' \times 19'$ area maps at 7 mm wavelength, centered on $[l, b] = [348.43, 0.16]$, to produce a data cube with 2 spatial and 1 spectral (velocity) dimension. The scan length was $15.6''$ per cycle time (of 2.0 s) and the spacing between scan rows was $26''$. Deep ON-OFF switched pointings were

Table 1. A summary of previous HI absorption analyses towards CTB 37A.

Gas Velocity (km s^{-1})	Absorption?	Relation to CTB 37A
-22	✓	Foreground ^{1,2}
-65	partial	Background/Some Foreground ^{1,2}
-85	✓	Foreground ^{1,2}
-110	✓	Foreground ^{1,2}
-145	×	Background ²

¹Caswell et al. (1975), ²Tian & Leahy (2012)

Table 2. The window set-up for the Mopra Spectrometer (MOPS) at 7 mm. The centre frequency, targeted molecular line, targeted frequency and total efficiency-corrected map noise (T_{RMS}) are displayed.

Centre Frequency (GHz)	Molecular Emission Line	T_{RMS} (K ch^{-1})	Detected? (Map/Point)
42.310	³⁰ SiO(J=1-0,v=0)	0.07	× ×
42.500	²⁸ SiO(J=1-0,v=3)	0.07	× ×
42.840	²⁸ SiO(J=1-0,v=2)	0.07	× ×
"	²⁹ SiO(J=1-0,v=0)	"	× ×
43.125	²⁸ SiO(J=1-0,v=1)	0.07	× ×
43.255	-	0.07	
43.395	²⁸ SiO(J=1-0,v=0)	0.07	× ✓
44.085	CH ₃ OH(7(0)-6(1) A++)	0.08	× ✓
44.535	-	0.08	
45.125	HC ₇ N(J=40-39)	0.09	× ×
45.255	HC ₅ N(J=17-16)	0.09	× ×
45.465	HC ₃ N(J=5-4,F=5-4)	0.09	✓ ✓
46.225	¹³ CS(1-0)	0.09	× ×
47.945	HC ₅ N(J=16-15)	0.12	× ×
48.225	C ³⁴ S(1-0)	0.12	× ×
48.635	OCS(J=4-3)	0.13	× ×
48.975	CS(1-0)	0.13	✓ ✓

also taken towards six locations (see Figure 1 and Table 3) containing 1720 MHz OH masers and one location centered on a peak of CS(1-0) emission seen in mapping data (Location 7). The naming convention for Locations 1-6 corresponds to the order of presentation of OH masers chosen from Table 2 of Frail et al. (1996). One 12 mm deep ON-OFF switched pointing was also performed towards the location $[l, b] = [348.37^\circ, 0.14^\circ]$ to follow up a feature discussed in § A. See Walsh et al. (2008) for the 12 mm spectrometer setup. We used a sky reference position of $[l, b] = [346.40, -1.64]$.

The Mopra spectrometer, MOPS, was employed and is capable of recording sixteen tunable, 4096-channel (137.5 MHz) bands simultaneously when in ‘zoom’ mode, as used here. A list of measured frequency bands, targeted molecular transitions and achieved T_{RMS} levels are shown in Tables 2 and 3.

The velocity resolution of the 7 mm zoom-mode data is $\sim 0.2 \text{ km s}^{-1}$. The beam FWHM and the pointing accuracy of Mopra at 7 mm are $59 \pm 2''$ and $\sim 6''$, respectively. The achieved T_{RMS} values for the total 7 mm map and individual pointings are stated in Tables 2 and 3, respectively.

OTF-mapping and deep ON-OFF switched pointing data were reduced and analysed using the ATNF anal-

ysis programs, LIVEDATA, GRIDZILLA, KVIS, MIRIAD and ASAP¹.

LIVEDATA was used to calibrate data against a sky reference position measured after each scan of a row/column was completed. A polynomial baseline-subtraction was also applied. GRIDZILLA then combined corresponding frequency bands of multiple OTF-mapping runs into 16 three-dimensional data cubes, converting frequencies into line-of-sight velocities. Data were then combined, weighting by the Mopra system temperature and smoothed in the Galactic $l - b$ plane using a Gaussian of FWHM $1.25'$.

MIRIAD was used to correct for the efficiency of the instrument (Urquhart et al. 2010) for mapping data and create line-of-sight velocity-integrated intensity images (moment 0) from data cubes.

ASAP was used to analyse deep ON-OFF switched pointing data. Data were time-averaged, weighted by system temperature and had fitted polynomial baselines subtracted. Like mapping data, deep pointing spectra were corrected for the Mopra beam efficiency (Urquhart et al. 2010). The beam efficiency for the CS(1-0) band for point and extended sources are ~ 0.43 and ~ 0.56 , respectively.

CO(2-1) data was taken with the Nanten2 4 m sub-millimeter telescope during December of 2008. The telescope has a beam FWHM of $\sim 90''$ at 230 GHz and a pointing accuracy of $\sim 15''$. The Acoustic Optical Spectrometer (AOS) had 2048 channels separated by 0.38 km s^{-1} , providing a bandwidth of 390 km s^{-1} . The achieved T_{RMS} was $\lesssim 0.7 \text{ K ch}^{-1}$. This CO(2-1) data offers superior spatial and velocity resolution when compared to previously-published CO(1-0) (Dame et al. 2001) data.

3 GAS PARAMETER CALCULATION

To address the amount of available hadronic target material towards HESS J1714–385, the column density towards absorbed X-ray sources and the density towards the observed OH masers, we calculated column density, mass and density using CO(2-1), CS(1-0) and HI data. As we discuss in §4, the gas observed towards CTB 37A appears extended, so we integrate our spectral line maps over a spatially wide region ($[\alpha, \delta]$ -space) to estimate average gas parameters within chosen regions. We used the MIRIAD functions *moment 0* and *mbspect* to calculate integrated intensity, $\int_V T_b dv_{\text{LSR}} d\alpha d\delta$ ($\text{K km s}^{-1} \text{ deg}^2$), and produce spectral line maps.

The mass of gas within the region, M , is related to the average column density, $\overline{N_{H_2}}$, by

$$M = 2m_H \overline{N_{H_2}} A \quad (1)$$

where A is the cross-sectional area of the region and $2m_H$ is the mass of molecular hydrogen. The average density, $\overline{n_{H_2}}$, was estimated by assuming that the thickness of the region in the line of sight direction was of the same order as the height and width, $\sim \sqrt{A}$.

3.1 CO

We scaled our CO(2-1) emission by the expected CO(1-0)/CO(2-1) intensity ratio,

$$\frac{W_{1-0}}{W_{2-1}} \approx \frac{1}{4} \exp \left[\frac{11.07 \text{ K}}{T_{\text{rot}}} \right] \quad (2)$$

where T_{rot} is the rotational temperature, which we assume to be 10 K. This allowed us to use the commonly cited/measured CO(1-0) X-factor, $X_{1-0} \sim 3 \times 10^{20} \text{ cm}^{-2} (\text{K km s}^{-1})^{-1}$ (Dame et al. 2001) to calculate H_2 column density, $N_{H_2} = X_{1-0} W_{1-0}$ from CO(2-1) intensity, W_{2-1} . Note, that a $0.7\text{-}3\times$ systematic error in column density would be introduced for a 5 K error in temperature estimation (using Equation 2). In an extreme case, such as $T = 40 \text{ K}$, like towards the shock of similar SNR, SNR W28 (Nicholas et al. 2011), we would expect the column density calculated from CO(2-1) using our method to change by a factor ~ 0.4 .

3.2 CS

We calculate the CS($J=1$) column density using Equation 9 from Goldsmith & Langer (1999). This equation requires an optical depth, which would usually be estimated from the CS(1-0)-C³⁴S(1-0) intensity ratio, but as we do not detect C³⁴S(1-0), for simplicity we assume that the CS(1-0) emission is optically thin ($\tau \rightarrow 0$). It follows that the column densities calculated from CS(1-0) may be considered as lower limits.

An LTE assumption at $T_{\text{rot}} \sim 10 \text{ K}$ implies that the total CS column density is simply a factor ~ 3.5 times the CS($J=1$) column density, and the molecular abundance of CS with respect to hydrogen is assumed to be $\sim 10^{-9}$ (Frerking et al. 1980). The systematic error introduced into the CS(1-0) column density by our temperature assumption is likely to be even smaller than that introduced for CO(2-1), with a 50% temperature systematic corresponding to a factor 0.7-1.2 error in column density. In the extreme case of $T = 40 \text{ K}$, column density calculated from CS(1-0) using our method changes by ~ 1.8 times.

3.3 HI

HI data is available (McClure-Griffiths et al. 2005; Haverkorn et al. 2006), and exhibits emission and absorption features towards CTB 37A. Where the level of radio continuum-absorption appears minor and HI emission is present, we constrain column density using an HI X-factor, $X_{HI} = 1.823 \times 10^{18} \text{ cm}^{-2} (\text{K km s}^{-1})^{-1}$ (Dickey & Lockman 1990).

For absorption lines, we first estimate an optical depth, $\tau \sim \ln(T_0/T_b)$, where T_0 is the continuum intensity and T_b is the local minimum intensity of an absorption line. This allows the calculation of atomic column density, $N_H \sim 1.9 \times 10^{18} \tau \Delta v_{\text{FWHM}} T_s$, where Δv_{FWHM} is an approximated full-width-half-maximum and T_s is the spin temperature, assumed to be 100 K. Since the calculated column density is proportional to the spin temperature, the uncertainty in column density due to our assumed temperature is the percentage as the uncertainty in temperature.

¹ See <http://www.atnf.csiro.au/computing/software/>

4 THE SPATIAL GAS DISTRIBUTION

Figure 2 is a longitude-velocity plot of CO(2-1) and CS(1-0) data (see Figure B1 for a latitude-velocity plot). Several clouds are visible in CO(2-1) and CS(1-0) emission at approximate line-of-sight reference velocities, $v_{\text{LSR}} \sim 5, -10, -22, -60$ to $-75, -90$ and -105 km s^{-1} . Additionally, SiO(1-0), $\text{HC}_3\text{N}(J=5-4)$ and $\text{CH}_3\text{OH}(7(0)-6(1) A++)$ were detected towards ‘Location 3’ (Figure 5) at velocity, $v_{\text{LSR}} \sim -105 \text{ km s}^{-1}$. Gaussian line fit parameters to the most significant emission lines are presented in Table 3.

Together, Mopra CS(1-0), Nanten CO(2-1) and SGPS HI data (McClure-Griffiths et al. 2005; Haverkorn et al. 2006) towards seven CTB 37A locations are shown in Figures 3-10. The HI data contained a strong radio continuum component from CTB 37A, producing absorption lines in foreground gas.

4.1 Gas Morphology

Referring to Moriguchi et al. (2005), which addresses CO(1-0) emission from the nearby SNR RX J1713.7–3946, regions traced by CO(2-1) and CS(1-0) may correspond to local gas ($\sim 5 \text{ km s}^{-1}$), the Sagittarius arm (~ -5 to -30 km s^{-1}), the Norma arm (~ -60 to -75 km s^{-1}), ‘Cloud A’ (~ -80 to -95 km s^{-1} , Slane et al., 1999) and the 3 kpc expanding arm (~ -100 to -115 km s^{-1}). Modeling by Vallee (2008) is not necessarily consistent with this scenario, with Figure 3d illustrating a model with possible gas components of the Sagittarius-Carina, Scutum-Crux and Norma-3 kpc arms present at velocities $v_{\text{LSR}} \sim -30$ to 0 km s^{-1} towards CTB 37A (Vallee also unified the various naming conventions for different components of single arms, including the Norma and 3 kpc arms which were part of the same structure). For velocities less than $v_{\text{LSR}} \sim -40 \text{ km s}^{-1}$, the model may predict the presence of components of the Perseus and Norma-3 kpc arms, but, as discussed by the authors, the model is less reliable towards the central 22° of the Galactic plane, so we do not attempt to rectify it with our observations.

In contrast to the above discussion, TL2012 make a case for the gas at -20 km s^{-1} and -60 km s^{-1} to both be associated with CTB 37A (i.e. present in the same arm) and within the inner 3 kpc of the galaxy (from HI-absorption arguments, see § 1.1).

All CO(2-1) emission in Figure 2 appears to have corresponding CS(1-0) emission, indicating dense gas. CS(1-0) and CO(2-1) emission integrated around the two separate populations of OH masers at $v_{\text{LSR}} \sim -22$ and -65 km s^{-1} are displayed in Figures 4a and b. Figures 4c and d display two other regions of gas along the line of sight that appear in HI absorption. In Figure 4, CS(1-0) emission peaks in regions displaying intense CO(2-1) emission. We investigate the association of this gas with CTB 37A and G348.5–0.0 in the following sections.

4.2 G348.5–0.0 and Interstellar Gas at $v_{\text{LSR}} = -25$ to -20 km s^{-1}

Figure 4a shows CS emission integrated over a velocity containing two 1720 MHz OH masers at $v_{\text{LSR}} \sim -23$ and

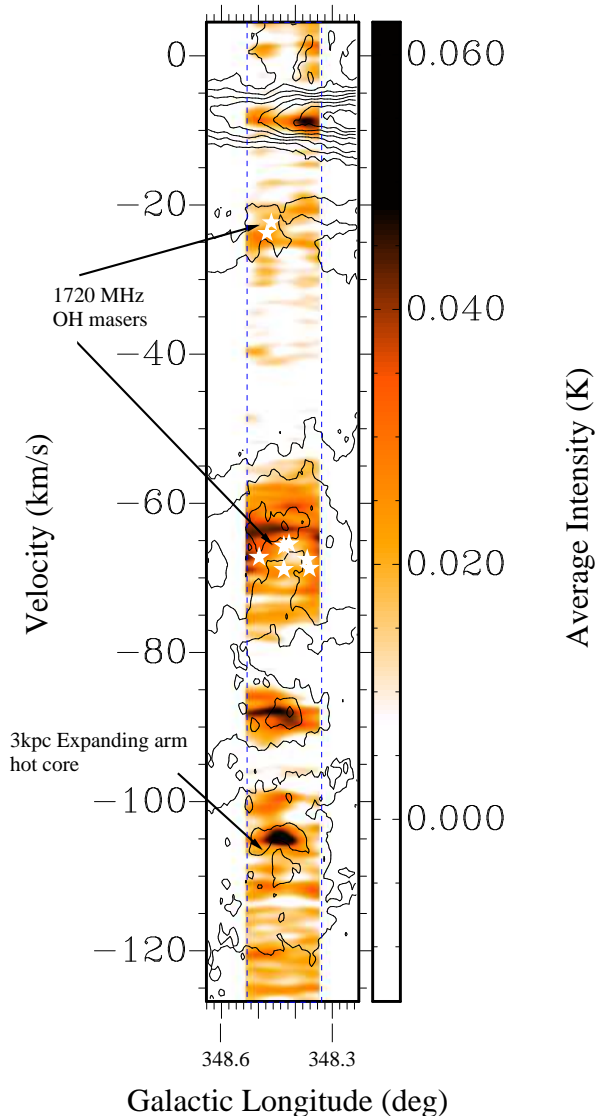


Figure 2. Position-velocity image of Mopra CS(1-0) emission towards the CTB 37A region. Nanten CO(2-1) emission contours towards the CTB 37A region are overlaid. White stars indicate 1720 MHz OH maser locations and the dashed lines indicate the extent of the 7 mm mapping campaign for CS(1-0) emission. A position-velocity image for the latitudinal gas distribution is displayed in the appendix (§B1). The image has been smoothed for clarity.

$\sim -21 \text{ km s}^{-1}$ (Frail et al. 1996). The CS(1-0) emission is coincident with these OH masers and a CO(2-1) emission peak and is somewhat extended, spanning $\sim 240''$ ($\sim 4 \times$ Beam FWHM) in length. Also note that the CS(1-0) emission peak may lie on the edge of G348.5–0.0, as approximately extrapolated from the partial shell observed in 843 MHz continuum data (see Figure 1). This is consistent with the $v_{\text{LSR}} \sim -22 \text{ km s}^{-1}$ masers being a product of a G348.5–0.0 shock-interaction towards a region of high density.

Figure 3 displays CO(2-1), CS(1-0) and HI (and continuum) data towards ‘Location 5’, which contains the $v_{\text{LSR}} \sim -22 \text{ km s}^{-1}$ population of 1720 MHz OH masers. CS(1-0) emission corresponds to at least three of the most

Table 3. Detected molecular transitions from deep ON-OFF switched pointings. Velocity of peak, v_{LSR} , peak intensity, T_{Peak} , and FWHM, Δv_{FWHM} , were found by fitting Gaussian functions before deconvolving with MOPS velocity resolution. Displayed band noise, T_{RMS} , and peak temperatures take into account beam efficiencies and contain a $\sim 5\%$ systematic uncertainty (Urquhart et al. 2010), after a baseline subtraction.

Object (l,b)	Detected Emission Line	T_{RMS} (K ch^{-1})	Peak v_{LSR} (km s^{-1})	T_{Peak} (K)	Δv_{FWHM} (km s^{-1})	Counterpart
Location 1 (348.35,0.18)	CS(1-0)	0.05	-73.4 ± 0.5	0.13 ± 0.01	18.9 ± 1.7	-65.1 km s^{-1} OH maser
Location 2 (348.35,0.15)	CS(1-0)	0.06	2.87 ± 0.08	0.41 ± 0.02	3.6 ± 0.2	-65.2 km s^{-1} OH maser
	HC ₃ N(J=5-4,F=5-4)	0.05	4.7 ± 0.2	0.12 ± 0.03	1.9 ± 0.6	
Location 3 (348.42,0.11)	CS(1-0)	0.05	-105.1 ± 0.03	0.78 ± 0.02	2.5 ± 0.1	-63.8 km s^{-1} OH maser ^a
			-88.0 ± 0.01	0.21 ± 0.02	1.6 ± 0.2	
			-57.6 ± 0.4	0.17 ± 0.01	21.8 ± 1.1	
			-22.4 ± 0.5	0.10 ± 0.07	9.2 ± 1.4	
	SiO(J=1-0,v=0)	0.03	-104.6 ± 0.3	0.06 ± 0.01	4.4 ± 1.2	
	HC ₃ N(J=5-4,F=5-4)	0.03	-104.8 ± 0.1	0.20 ± 0.01	2.7 ± 0.3	
	CH ₃ OH(7(0,7)-6(1,6) A++)	0.03	-104.4 ± 0.1	0.13 ± 0.01	1.9 ± 0.2	
Location 4 (348.39,0.08)	CS(1-0)	0.04	-61.9 ± 0.6	0.07 ± 0.01	12.1 ± 1.8	-63.5 km s^{-1} OH maser
			-21.9 ± 0.2	0.13 ± 0.02	1.5 ± 0.3	
			8.3 ± 0.1	0.14 ± 0.02	1.5 ± 0.3	
Location 5 (348.48,0.11)	CS(1-0)	0.04	-23.0 ± 0.1	0.18 ± 0.02	3.1 ± 0.4	-23.3 km s^{-1} OH maser ^a
Location 6 (348.51,0.11)	CS(1-0)	0.07	-63.9 ± 0.2	0.23 ± 0.02	7.4 ± 0.6	-64.3 km s^{-1} OH maser
Location 7 (348.32,0.23)	CS(1-0)	0.05	-103.9 ± 0.1	0.26 ± 0.02	1.7 ± 0.2	
			-89.2 ± 0.2	0.16 ± 0.02	3.7 ± 0.4	
			-64.2 ± 0.1	0.41 ± 0.01	6.1 ± 0.3	

^aPointing has partial overlap with a second 1720 MHz OH maser of similar v_{LSR} .

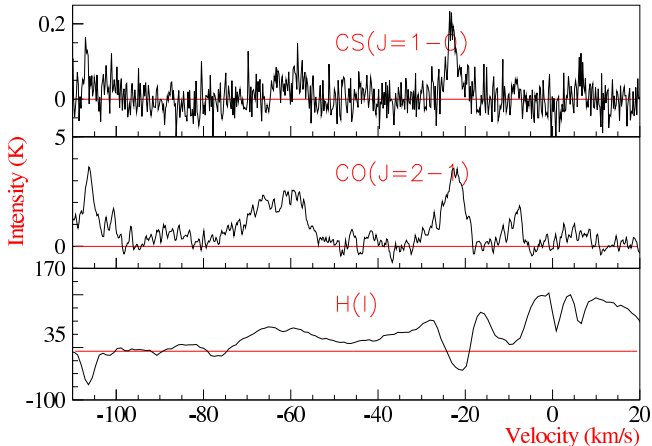


Figure 3. Location 5: This region encompasses two 1720 MHz OH masers. One is at velocity $v_{\text{LSR}} \sim -23.3 \text{ km s}^{-1}$ (the centre of the pointing location) and another velocity $v_{\text{LSR}} \sim -21.4 \text{ km s}^{-1}$ (offset from the centre, but within the 7 mm beam FWHM solid angle). See Table 3 and Figure 1b for further details.

intense CO(2-1) peaks ($v_{\text{LSR}} \sim -22, -65, -105 \text{ km s}^{-1}$). The strongest CS(1-0) emission peak towards this location is at velocity $v_{\text{LSR}} \sim -23 \text{ km s}^{-1}$, consistent with the velocity of the OH masers. A distinct HI absorption line also corresponds to the dense and masing gas at $v_{\text{LSR}} \sim -22 \text{ km s}^{-1}$. This implies that the gas is likely foreground to the radio

continuum emission from this region. It follows that if the radio continuum emission seen towards Location 5 is indeed from CTB 37A, the $v_{\text{LSR}} \sim -22 \text{ km s}^{-1}$ gas (and associated OH maser population) lies in front of CTB 37A. Similar $v_{\text{LSR}} \sim -22 \text{ km s}^{-1}$ HI absorption features are observed towards Locations 3, 4 and 6 (Figures 5, 6 and 7, respectively). These positions are, unlike Location 5, not towards regions of suspected SNR-SNR-overlap, only SNR CTB 37A.

The $v_{\text{LSR}} \sim -22 \text{ km s}^{-1}$ gas may be shocked by either CTB 37A or G348.5-0.0. In the former case, the gas would not be at its kinematic distance (possibly within the 3 kpc ring instead), while CTB 37A would be between the foreground $v_{\text{LSR}} \sim -22 \text{ km s}^{-1}$ gas and the background/associated $v_{\text{LSR}} \sim -65 \text{ km s}^{-1}$ gas.

In the latter case (a G348.5-0.0- $v_{\text{LSR}} \sim -22 \text{ km s}^{-1}$ maser/gas association), the Galactic rotation model distance may hold for the $v_{\text{LSR}} \sim -22 \text{ km s}^{-1}$ gas, favouring a near-side distance solution of $\sim 3 \text{ kpc}$ for the $v_{\text{LSR}} \sim -22 \text{ km s}^{-1}$ masers, molecular gas and G348.5-0.0. It is unclear from current evidence which of the two scenarios is valid, but 1720 MHz OH maser emission from SNRs is relatively rare, with only $\sim 10\%$ of surveyed SNRs having detectable OH masers (Green et al. 1997). Although the Green et al. survey did target (hence is biased towards) SNRs with a central thermal X-ray source, one might naively suggest, post-priori, that the likelihood of G348.5-0.0 producing OH maser emission is about 10%, with the more likely cause of $v_{\text{LSR}} \sim -22 \text{ km s}^{-1}$ OH maser generation being an inter-

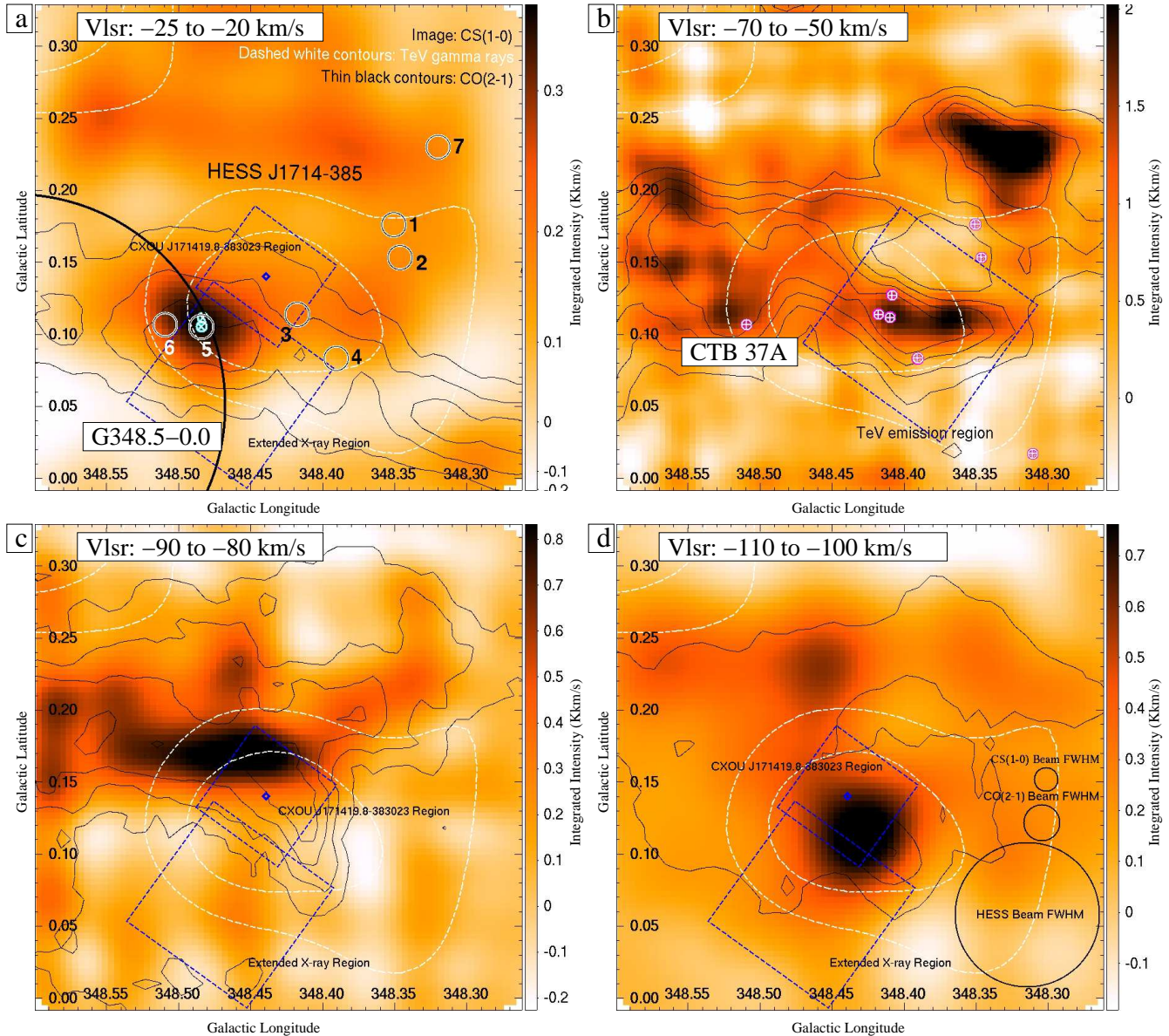


Figure 4. Mopra CS(1-0) emission images with overlaid Nanten2 CO(2-1) contours (black) for four different velocity ranges (panels a-d). CS(1-0) emission in all figures has been Gaussian-smoothed (FWHM \sim 30-90''). All figures have overlaid HESS 80 and 100 gamma-ray excess count contours (dashed white lines) (Aharonian et al. 2008a). (a) CO contour levels are from 5 to 20 K km s $^{-1}$ in steps of 5 K km s $^{-1}$. The approximate location of G348.5-0.0 is indicated by a black circle (partially shown). Two blue dashed boxes represent regions used to calculate gas parameters (see § 5.1, also in c and d). Deep switched pointing locations are displayed as circles and 1720 MHz OH masers at the velocity of the CS(1-0) emission are indicated by blue crosses. (b) CO contour levels are from 24 to 48 K km s $^{-1}$ in steps of 8 K km s $^{-1}$. A large blue dashed box (TeV emission) represent a region used to calculate gas parameters (see § 5.2). 1720 MHz OH masers at the velocity of the CS(1-0) emission are indicated by pink crosses. (c) CO contour levels are from 5 to 20 K km s $^{-1}$ in steps of 5 K km s $^{-1}$. (d) CO contour levels are from 10 to 30 K km s $^{-1}$ in steps of 10 K km s $^{-1}$. The beam FWHM for HESS, Mopra and Nanten2 observations are indicated.

action between SNR CTB 37A and a second molecular gas clump of a different local velocity (the $v_{\text{LSR}} \sim 22$ km s $^{-1}$ gas). The work by TL2012 does seem to support the notion that the kinematic distances of these gas components are not reliable.

An estimation of mass and density at $v_{\text{LSR}} \sim -22$ km s $^{-1}$ towards Location 5 can be found using Equation 1, where A is set equal to the Mopra beam FWHM area (at some assumed distance). For CS(1-0) emission, this yields a column density of $N_{\text{H}_2} \sim 1 \times 10^{22}$ cm $^{-2}$, which implies a mass

of $\sim 400 M_{\odot}$ and density of $\sim 1 \times 10^3$ cm $^{-3}$ at a distance of 7.9 kpc (or $\sim 40 M_{\odot}$ and $\sim 5 \times 10^3$ cm $^{-3}$ at a distance of 3 kpc, if G348.5-0.0 produced the $v_{\text{LSR}} \sim -22$ km s $^{-1}$ masers). This density is not as high as the $\sim 10^4$ - 10^5 cm $^{-3}$ suspected to be required for the formation of 1720 MHz OH masers (Reynoso & Mangum 2000), but our result does not rule out this density on a scale smaller than our 7 mm beam (~ 2 pc at 7.9 kpc), as expected for the maser-emission region size. Indeed, given that the CS(1-0) critical density is $\sim 8 \times 10^4$ cm $^{-3}$, its likely that the beam is only partially-

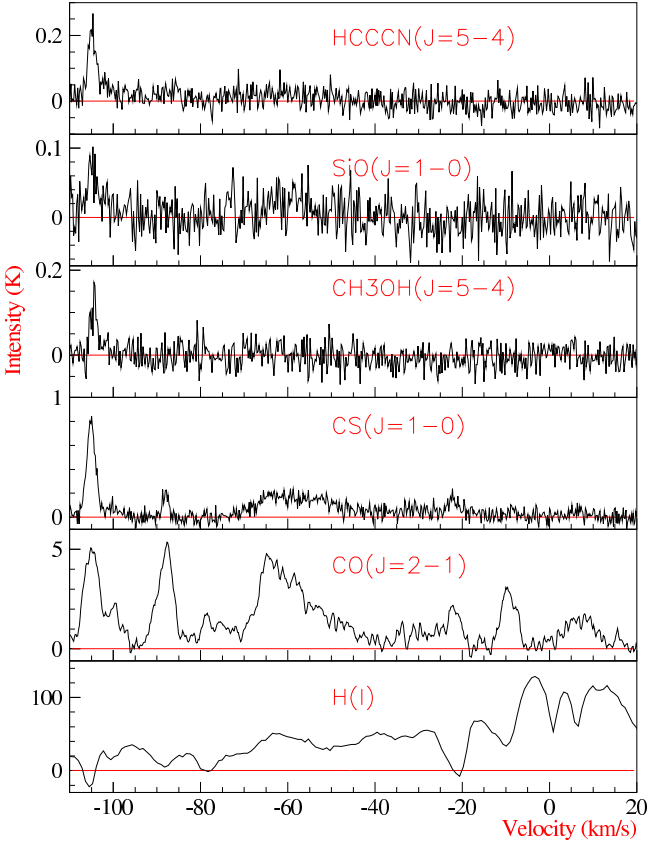


Figure 5. Location 3: This region encompasses two 1720 MHz OH masers. One is at velocity $v_{\text{LSR}} \sim -63.8 \text{ km s}^{-1}$ (the centre of the pointing location) and another velocity $v_{\text{LSR}} \sim -63.9 \text{ km s}^{-1}$ (offset from the centre, but within the 7 mm beam FWHM solid angle). See Table 3 and Figure 1b for further details.

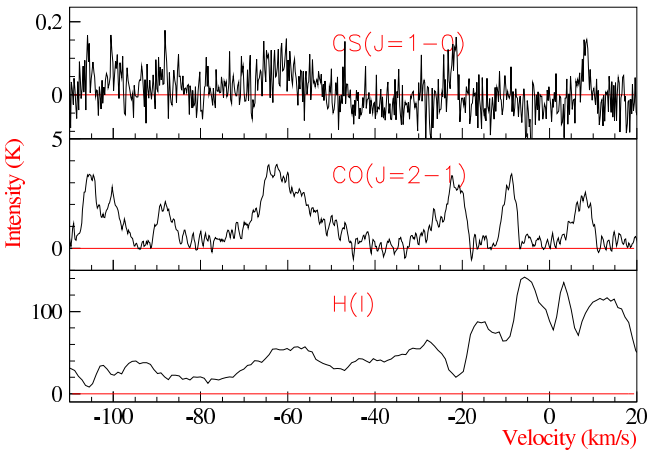


Figure 6. Location 4: This region encompasses one 1720 MHz OH maser at velocity $v_{\text{LSR}} \sim -63.5 \text{ km s}^{-1}$. See Table 3 and Figure 1b for further details.

‘filled’. Additionally, we have used an ‘optically-thin’ assumption (see §3), but the region could indeed be more optically deep, hence have a higher column density than what we have calculated.

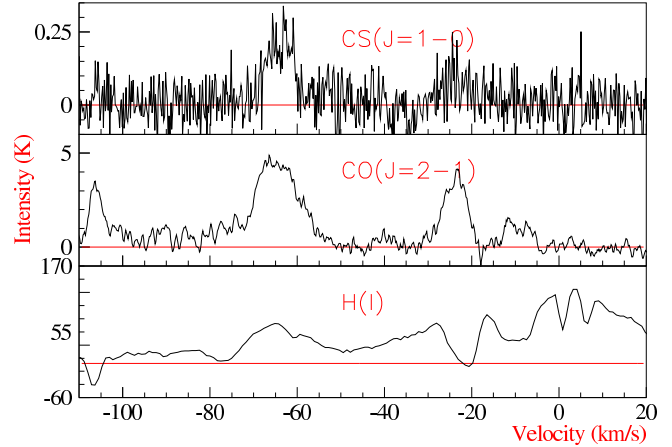


Figure 7. Location 6: This region encompasses one 1720 MHz OH maser at velocity $v_{\text{LSR}} \sim -64.3 \text{ km s}^{-1}$. See Table 3 and Figure 1b for further details.

4.3 CTB 37A and Interstellar Gas at $v_{\text{LSR}} = -70$ to -50 km s^{-1}

Figure 4b shows CS(1-0) emission integrated over a velocity consistent with eight 1720 MHz OH masers between $v_{\text{LSR}} \sim -70$ and $\sim -60 \text{ km s}^{-1}$ (Frail et al. 1996). Broad CS(1-0) emission is seen towards regions with intense CO(1-0) emission. Some of the gas in this field is believed to be associated with the CTB 37A SNR and the $\sim -60 \text{ km s}^{-1}$ masers, which are in the inner 3 kpc of the Galaxy (between 6.3 kpc and 9.5 kpc, TL2012).

The existence of a shocked or energetic environment at $v_{\text{LSR}} \sim -65 \text{ km s}^{-1}$, possibly triggered by CTB 37A, is indicated by the extreme broadness of the CO(2-1) and CS(1-0) line spectra and clear asymmetries in CO(2-1) emission towards Locations 3 and 4 (Figures 5 and 6). In such environments, the detection of SiO emission can sometimes be expected as Si is sputtered from dust grains, but the only signal corresponding to CTB 37A from this shock-tracer was tenuous. A fit to the SiO(1-0) spectrum towards Location 3 (Figure 5, Table 3) at $v_{\text{LSR}} \sim -60 \text{ km s}^{-1}$ (guided by the broad CS(1-0) emission) yielded a line FWHM of $\sim 19 \pm 5 \text{ km s}^{-1}$, consistent with a shocked or turbulent region. This detection, albeit weak, may support the connection of the $v_{\text{LSR}} \sim -65 \text{ km s}^{-1}$ gas to the CTB 37A SNR.

Via CS(1-0) emission we can confirm the existence of dense gas-associations with $v_{\text{LSR}} \sim -65 \text{ km s}^{-1}$ OH masers towards locations 3, 4 and 6. We estimate, column densities, masses and densities from CS(1-0) of $\sim 1-8 \times 10^{22} \text{ cm}^{-2}$, $\sim 500-2300 M_{\odot}$ and $\sim 3-10 \times 10^3 \text{ cm}^{-3}$, respectively, at these three locations (with assumptions outlined in §3). These densities are, similar to the previous calculation (see §4.3), not as high as the $\sim 10^4-10^5 \text{ cm}^{-3}$ suspected to be required for the formation of 1720 MHz OH masers. This does not rule out a density of $\sim 10^4-10^5 \text{ cm}^{-3}$ on a scale smaller than our 7 mm beam ($\sim 2 \text{ pc}$ at 7.9 kpc).

Towards locations 1 and 2, no CS(1-0) emission was confirmed above the noise level of $\sim 0.05 \text{ K}$, so like Reynoso & Mangum (2000), we are unable to give evidence of a dense-molecular gas association towards the OH masers at these two positions. Lastly, we note that towards these two positions, a shell-like structure of radius $\sim 0.025^{\circ}$ cen-

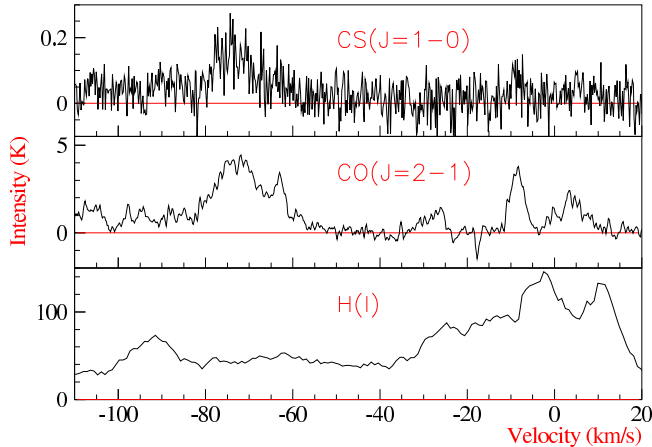


Figure 8. Location 1: This region encompasses one 1720 MHz OH maser at velocity $v_{\text{LSR}} \sim -65.1 \text{ km s}^{-1}$. See Table 3 and Figure 1b for further details.

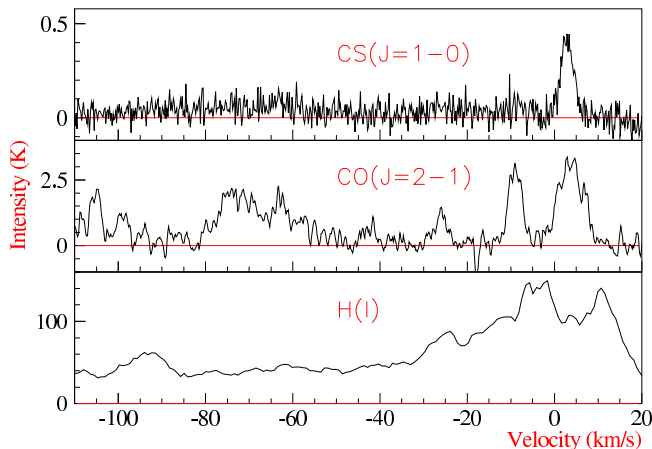


Figure 9. Location 2: This region encompasses one 1720 MHz OH maser at velocity $v_{\text{LSR}} \sim -65.2 \text{ km s}^{-1}$. See Table 3 and Figure 1b for further details.

tred near $[l,b] \sim [348.37, -0.16]$ appears to exist in CS(1-0) and CO(2-1) emission. We are unable to determine the cause of this void in molecular emission, but this may be a low gas density cavity blown out by a SNR or SNR progenitor star wind. Furthermore, we note a distinct lack of molecular gas to the South of CTB 37A, so we are unable to add more to the discussion of the break-out morphology of CTB 37A.

4.4 Interstellar Gas at $v_{\text{LSR}} = -90$ to -80 km s^{-1}

Figure 4c is an integrated image of the CS(1-0) and CO(2-1) emission around $v_{\text{LSR}} = -85 \text{ km s}^{-1}$. Some HI-absorption at $v_{\text{LSR}} \sim -85 \text{ km s}^{-1}$ is present towards Location 3 (Figure 5). This is evidence that the $v_{\text{LSR}} \sim -85 \text{ km s}^{-1}$ gas is foreground to CTB 37A, but this is not especially useful in distinguishing whether this gas is associated with the CTB 37A SNR (including whether this cloud is experiencing a high energy particle enhancement caused by CTB 37A). It follows that we consider both of two scenarios: an association of this gas with the gamma-ray emission and no association of this gas with the gamma-ray emission in §5.2. This gas appears

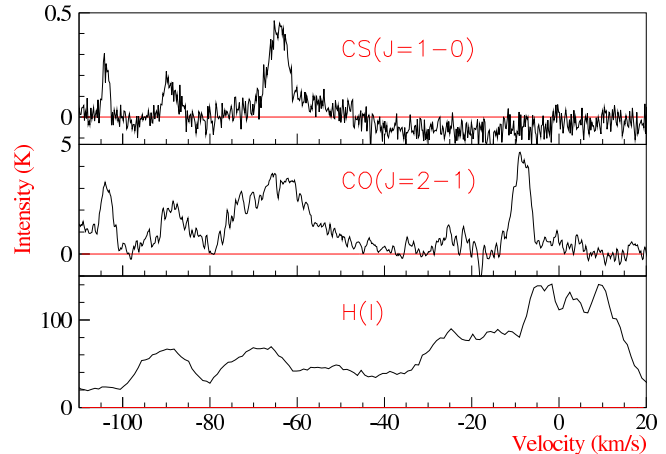


Figure 10. Location 7: See Table 3 and Figure 1b for further details.

at the same velocity as ‘Cloud A’ (Slane et al. 1999), which can be seen to extend over 1° in longitude (Moriguchi et al. 2005), suggesting a possible relation.

4.5 Interstellar Gas at $v_{\text{LSR}} = -110$ to -100 km s^{-1}

Gas from the near side of the 3kpc-expanding-arm is observed at $v_{\text{LSR}} \sim -105 \text{ km s}^{-1}$ in the direction of CTB 37A, as displayed in Figure 4d. The significance of this gas to the present study is a correspondence with HI absorption in the CTB 37A radio continuum (see §1.1). CS(1-0) and CO(2-1) emission peak at a position overlapping Location 3 at $v_{\text{LSR}} \sim -105 \text{ km s}^{-1}$. CS(1-0) and $\text{HC}_3\text{N}(J=5-4)$ emission indicates that the gas is dense (CS(1-0) emission $\Rightarrow n_{\text{H}_2} \sim 7 \times 10^3 \text{ cm}^{-3}$, see Table 6), while $\text{CH}_3\text{OH}(7(0)-6(1) \text{ A}++)$ emission suggests the presence of high-temperature chemistry often associated with star-formation (van Dishoeck & Blake 1998). SiO(1-0) emission is also associated with this clump, implying the existence of shocked gas. Although this might be considered evidence for a SNR shock-gas interaction, the coinciding tracers (CS, HC_3N and CH_3OH) can also frame a picture consistent with in/outflows associated with star-formation (see Figure B2 for SiO, HC_3N and CH_3OH emission maps). Indeed, this narrow SiO(1-0) spectrum does not share similarities with shocked gas towards the similar SNR W28, where broad SiO emission is observed at a position/velocity consistent with OH maser emission (Nicholas et al. 2012). We display the discovered SiO, HC_3N and CH_3OH emission and investigate possible infrared counterparts in appendices (§A and §B).

Table 4. Gas parameters towards a rectangular region of sky containing the HESS J1714-385 68% containment region defined as “TeV emission” (see Figure 4b), extended X-ray emission and a PWN candidate source, CXOU J171419.8–383023, (see Figures 4a, c and d) (Aharonian et al. 2008a). CO(2-1) and CS(1-0)-derived average column density, N_{H_2} , mass, M , and average density, n_{H_2} , within the selected region are shown for chosen velocity ranges. All calculated values have an associated statistical uncertainty of $\sim 10\%$.

Region	Velocity Range (km s ⁻¹)	Assumed Distance, d_0 (kpc) ^b	$\overline{N_{H_2}}$ (10 ²¹ cm ⁻²)	CO(2-1) M (M _⊙)	$\overline{n_{H_2}}$ (cm ⁻³)	$\overline{N_{H_2}}$ (10 ²¹ cm ⁻²)	CS(1-0) M (M _⊙)	$\overline{n_{H_2}}$ (cm ⁻³)
TeV emission ^a	-25 to -20	7.9	1.5 ^{+0.2} _{-0.2}	9 000 ^{+5 000} _{-6 000}	30 ⁺²⁰ ₋₂₀	0.3 ^{+0.1} _{-0.05}	1 000 ^{+1 000} ₋₂₀₀	6 ⁺⁷ ₋₂
	-70 to -50	7.9	3.9 ^{+1.2} _{-0.6}	30 000 ^{+15 000} _{-17 000}	90 ⁺⁹⁰ ₋₆₀	1.3 ^{+0.8} _{-0.2}	6 000 ^{+2 000} _{-2 000}	30 ⁺³⁰ ₋₁₀
	-90 to -80	7.9	1.2 ^{+0.3} _{-0.2}	8 000 ^{+30 000} _{-5 000}	20 ⁺³⁰ ₋₁₀	0.2 ^{+0.05} _{-0.1}	700 ^{+1 000} ₋₇₀₀	3 ⁺¹ ₋₃
	Sum of the above		8.1 ^{+1.7} _{-0.9}	47 000 ^{+23 000} _{-27 000}	-	1.8 ⁺¹ _{-0.4}	8 000 ^{+4 000} _{-3 000}	
	-110 to -100	6.3	2.1 ^{+0.6} _{-0.3}	8 000 ^{+3 000} _{-3 000}	30 ⁺⁵⁰ ₋₂₀	0.9 ^{+0.1} _{-0.2}	2 000 ^{+1 000} _{-1 000}	20 ⁺²⁰ ₋₁₀
Extended	-25 to -20	7.9	1.8	5 000	50	0.3	900	6
X-ray emission	-70 to -50	7.9	3.2	9 000	80	0.8	3 000	20
	-90 to -80	7.9	0.5	1 000	10	0.2	700	5
	-110 to -100	6.3	1.4	3 000	50	0.8	2 000	20
CXOU J171419.8 -383023	-25 to -20	7.9	1.7	3 000	60	0.4	700	10
	-70 to -50	7.9	7.1	10 000	240	1.8	3 000	60
	-90 to -80	7.9	2.1	3 000	80	1.1	2 000	40
	-110 to -100	6.3	3.0	3 000	120	1.5	1 000	60

^a Super/subscripts indicate uncertainty propagated from the 1' uncertainty in the 68% containment radius of HESS J1714–385.

^b Distances are assumed for mass and density calculations, but can be scaled from the assumed distance, d_0 , to a different distance, d , by multiplying by $(d/d_0)^2$ and $(d/d_0)^{-1}$ for mass and density, respectively, if further distance constraints arise in the future.

5 DISCUSSION

5.1 Previous X-ray Absorption Studies

CTB 37A exhibits extended thermal X-ray emission, possibly from a SNR shock-gas interaction, and a more compact non-thermal source, CXOU J171419.8–383023 (Chandra beam FWHM $\sim 1''$), which may be a PWN (Aharonian et al. 2008a). Aharonian et al. (2008a) used a spectral-fitting analysis technique to estimate the level of X-ray-absorption, and hence the column density towards these two sources. We compare column densities estimated from CO(2-1), CS(1-0) and HI data to column densities calculated from X-ray absorption. The column densities and masses of significant molecular and atomic gas foreground to the CTB 37A extended X-ray emission and CXOU J171419.8–383023 are presented in Tables 4 and 5. The X-ray emission regions are highlighted in Figures 4a, c and d.

Towards the extended thermal X-ray emission region, we calculated a lower limit for proton column density ($\overline{N_H} + 2\overline{N_{H_2}}$, where $\overline{N_{H_2}}$ is the average of that derived for CO(2-1) and CS(1-0)) of $\sim 9 \times 10^{21} \text{ cm}^{-2}$. Aharonian et al. (2008a) calculated an X-ray absorption proton column density of $\sim 3 \times 10^{22} \text{ cm}^{-2}$ consistent with our lower limit and work by Sezer et al. (2011).

Similar to towards the extended thermal X-ray emission region, towards CXOU J171419.8–383023, we calculated a lower limit on proton column density foreground to CTB 37A ($\overline{N_H} + 2\overline{N_{H_2}} \sim 1.5 \times 10^{22} \text{ cm}^{-2}$) that was consistent with the X-ray absorption proton column density of $\sim 6 \times 10^{22} \text{ cm}^{-2}$.

We note that the molecular gas fractions ($H_2/[H+H_2]$) for these two regions are $f_{H_2} \sim 0.38$ and ~ 0.47 . Liszt et al. (2010) investigated the atomic gas fraction from a sample of sources using HCO⁺ emission, CO emission and HI absorption and found that the molecular gas fraction was $f_{H_2} \sim 0.35$, i.e. $\sim 2 \times$ more atomic H atoms exist than H₂ molecules. The authors noted the results of other methods that put $f_{H_2} \gtrsim 0.25$ (Bohlin et al. 1978) and $f_{H_2} \approx 0.40-0.45$ (Liszt et al. 2002). Our calculated molecular gas fractions (0.38 and 0.47) are consistent with previous analyses, adding confidence to the accuracy of our column density estimations. There is, however, a factor $\sim 3-4$ difference between our lower limits on column density and the X-ray absorption column densities. This may be due to gas components being overlooked by our observation or analysis.

5.2 Towards HESS J1714–385

If the observed TeV emission is produced by hadronic processes (i.e. CR protons or nuclei colliding with matter to produce neutral pions that decay into gamma-ray photons), constraining the mass of matter may help to constrain the CR density in the region. Aharonian et al. (1991) derived a relation to predict the flux of gamma-rays from the mass of CR-target material, assuming an $E^{-1.6}$ integral power law spectrum. The expected gamma ray flux above E_γ is,

$$F(\geq E_\gamma) = 2.85 \times 10^{-13} E_{TeV}^{-1.6} \left(\frac{M_5}{d_{kpc}^2} \right) k_{CR} \text{ cm}^{-2} \text{ s}^{-1} \quad (3)$$

where M_5 is the gas mass in units of $10^5 M_\odot$, d_{kpc} is the distance in units of kpc, k_{CR} is the CR enhancement fac-

tor above that observed at Earth and $E_\gamma > 1 \text{ TeV}$. The gamma-ray flux above 1 TeV towards CTB 37A is $F(> 1 \text{ TeV}) \sim 6.7 \times 10^{-13} \text{ cm}^{-2} \text{ s}^{-1}$ (Aharonian et al. 2008a) and the masses within the HESS best fit region (68% containment of the gamma-ray source) were calculated for given velocity ranges (see Tables 4 and 5). The cosmic ray enhancement factor, k_{CR} , could thus be calculated for several velocity ranges. These are displayed in Table 7.

CR enhancement factor estimates (above 1 TeV) for the gas at $v_{LSR} \sim -22, -85$ and -110 km s^{-1} range between 320 and 33 000, whereas the CR enhancement factor estimate for the gas at $v_{LSR} \sim -60 \text{ km s}^{-1}$, the gas most likely to be associated with CTB 37A, generally spans a range of smaller values, 130–1 100. We assume that the gas at $v_{LSR} \sim -60 \text{ km s}^{-1}$ is associated with CTB 37A, while the gas components at $v_{LSR} \sim -22$ and -85 km s^{-1} may or may not additionally be associated, giving a range of possible CR-enhancements in the CTB 37A region of $\sim 80-1100 \times$ (see Table 7) that observed in the local solar neighbourhood, assuming a hadronic scenario.

In a hadronic scenario for gamma-ray production, matter is expected to overlap with gamma-ray emission on a large-scale, because the TeV gamma-ray flux is proportional to the product of mass, M_5 , and cosmic ray enhancement, k_{CR} . If one assumes a uniform CR-density throughout the CTB 37A region, a good correlation between matter density and hadronic gamma-ray emission might be expected, which, from CO(2-1) and CS(1-0) emission (see Figure 4), may be the case for line of sight velocity, $\sim -85 \text{ km s}^{-1}$, but less likely to be so for the line of sight velocities, $\sim -22 \text{ km s}^{-1}$ or $\sim -110 \text{ km s}^{-1}$. Gamma-ray flux variation can also reflect variation in cosmic ray enhancement, such that a region can have matter existing outside of the region indicated by gamma-ray emission contours (see Figure 4) while still being consistent with a hadronic emission scenario. With this in mind, the line of sight velocity $\sim -60 \text{ km s}^{-1}$, the suspected location of CTB 37A, is consistent with a hadronic scenario. When we summed multiple emission components, i.e. the $v_{LSR} \sim -22 \text{ km s}^{-1}$, -60 km s^{-1} and -85 km s^{-1} gas, the $v_{LSR} \sim -60 \text{ km s}^{-1}$ component is dominant, such that only minimal improvement in molecular gas-gamma ray overlap was observed. It seems that from studies of the overlap between molecular gas and gamma-ray emission alone, no clear conclusion about which gas clumps correspond to CTB 37A can be drawn.

The proportion of gas that may be acting as target material towards the HESS J1714–385 region is unknown, so CR enhancement estimates in Table 7 may be considered as lower than plausibly expected. Conversely, a component of dark gas (where carbon exists in an atomic/ionic form and hydrogen exists in molecular form) towards the HESS J1714–385 region is not taken into account (and may indeed exceed 30% according to Wolfire et al., 2010), making the CR enhancement estimates higher than plausibly expected. Due to these two unconstrained effects, CR enhancement estimates in Table 7 should be considered with some caution.

We note that towards the HESS J1714-385 TeV emission region, a calculation of the kinetic energy (Arikawa et al. 1999; Nicholas et al. 2011) implied by observed CS(1-0) emission at $v_{LSR} \sim -60 \text{ km s}^{-1}$, $E \sim \frac{1}{2} M \Delta v_{FWHM}^2$, is $\sim 0.4-4 \times 10^{50}$ erg. This is a significant frac-

Table 5. Same as Table 4, but parameters are from HI absorption analyses (and emission analyse where specified) and showing atomic (in contrast to molecular) H column density.

Region	Velocity Range (km s ⁻¹)	Assumed Distance, d_0 (kpc)	$\overline{N_H}$ (10 ²¹ cm ⁻²)	HI M (M _⊙)	$\overline{n_H}$ (cm ⁻³)
TeV emission	^a - 70 to -50	7.9	5.6 ^{+0.1} _{-0.1}	9 000 ⁺³⁰⁰⁰ ₋₆₀₀₀	130 ⁺¹⁰⁰ ₋₂₀
	5 to 8	-	0.3 ^{+0.1} _{-0.05}	-	-
	0 to 2	-	0.3 ^{+0.1} _{-0.05}	-	-
	-13 to -7	1.5	1.9 ^{+0.9} _{-0.3}	100 ⁺¹⁰⁰ ₋₀	200 ⁺²⁰⁰ ₋₁₀₀
	-24 to -18	7.9	2.8 ^{+1.8} _{-0.2}	6 000 ⁺³⁰⁰⁰ ₋₅₀₀	50 ⁺⁵⁰ ₋₁₀
	-74 to -71	7.9	0.1 ^{+0.05} _{-0.05}	300 ⁺¹⁰⁰ ₋₁₀₀	3 ⁺¹ ₋₁
	-90 to -86	7.9	0.2 ^{+0.0} _{-0.05}	400 ⁺²⁰⁰ ₋₂₀₀	4 ⁺¹ ₋₁
	-107 to -103	6.3	0.2 ^{+0.1} _{-0.0}	300 ⁺²⁰⁰ ₋₁₀₀	6 ⁺⁴ ₋₁
	Absorption sum			5.8 ^{+3.0} _{-0.4}	7 000 ⁺³⁰⁰⁰ ₋₁₀₀₀
Extended X-ray emission	^a - 70 to -50	7.9	4.6	5 000	100
	5 to 8	-	0.3	-	-
	0 to 2	-	0.4	-	-
	-13 to -7	1.5	1.0	50	100
	-23 to -18	7.9	1.2	2 000	30
	-79 to -76	7.9	0.2	300	4
	-92 to -87	7.9	0.3	500	8
	-107 to -104	6.3	0.6	500	20
	Absorption sum			4.0	-
CXOU J171419.8-383023	^a - 70 to -50	7.9	5.9	4 000	200
	5 to 8	-	0.2	-	-
	0 to 2	-	0.4	-	-
	-13 to -7	1.5	1.3	40	200
	-23 to -18	7.9	2.2	2 000	70
	-79 to -76	7.9	0.3	200	10
	-92 to -87	7.9	0.5	400	20
	-107 to -104	6.3	0.6	300	30
	Absorption sum			5.5	-

^aFrom HI emission analyses.**Table 6.** Gas parameters towards locations with ON-OFF switched deep CS(1-0) observations (see Figure 1). CS(1-0)-derived average column density, N_{H_2} , mass, M , and average density, n_{H_2} , within selected regions are shown for significant CS(1-0) emission lines (see Table 3). All calculated values have an associated statistical uncertainty of ~15%.

Location	Velocity (km s ⁻¹)	Assumed Distance (kpc)	$\overline{N_{H_2}}$ (10 ²¹ cm ⁻²)	CS(1-0) M (M _⊙)	$\overline{n_{H_2}}$ (cm ⁻³)
1	-73.4	7.9	49	1 500	7×10 ³
3	-105.1	6.3	39	800	7×10 ³
	-88.0	7.9	6.8	200	1×10 ³
	-57.6	7.9	75	2 300	1×10 ⁴
	-22.4	7.9	19	600	3×10 ³
4	-61.9	7.9	17	500	3×10 ³
	-21.9	7.9	3.9	100	600
5	-23.0	7.9	11	400	1×10 ³
6	-63.9	7.9	34	1 100	5×10 ³
7	-103.9	6.3	8.9	170	2×10 ³
	-89.2	7.9	1.2	370	2×10 ³
	-64.2	7.9	50	1 500	7×10 ³

Table 7. Atomic mass (from HI analyses), molecular mass (average of CO and CS analyses) are summed and multiplied by 1.33 to account for a 25% He component. The ranges displayed reflect the uncertainty in the 68% containment radius of HESS J1714-385. An estimate of CR enhancement factor above the solar system value (>1 TeV), k_{CR} , assuming that all mass coincident the best-fit region of HESS J1714-385 acts as CR target material, is also displayed.

Region Velocity Range (km s ⁻¹)	Assumed Distance, d_0 (kpc)	Atomic mass (M _⊙)	Molecular mass (M _⊙)	Total mass (25% He) (M _⊙)	$\sim k_{CR}^a$
TeV emission -25 to -20	7.9	5 500 - 9 000	800 - 14 000	8 400 - 31 000	320 - 1 200
-70 to -50	7.9	3 000 - 12 000	4 000 - 45 000	9 300 - 76 000	130 - 1 100
-90 to -80	7.9	200 - 600	0 - 11 000	300 - 15 000	660 - 33 000
Sum of the above		8 700 - 22 000	4 800 - 70 000	18 000 - 120 000	80 - 550
-110 to -100	6.3	200 - 500	1 000 - 11 000	1 600 - 15 000	420 - 6 200

^a CR enhancement factor is effectively independent of the assumed distance (as distance cancels in Equation 3 when the distance assumptions of our mass calculations are accounted for.)

tion (4-40%) of the assumed SNR ejecta kinetic energy of $\sim 10^{51}$ erg, so may in fact be injected by CTB 37A. The CS(1-0) emission at $v_{LSR} \sim -22$ km s⁻¹ is also broad, and implies a kinetic energy of $\sim 0.7 \cdot 3 \times 10^{49}$ erg, ~ 0.7 -3% of the assumed ejecta energy. Both the $v_{LSR} \sim -22$ and -60 km s⁻¹ gas clouds have velocity dispersions consistent with a SNR-shock interaction.

5.3 The Age of CTB 37A

The age of CTB 37A has been considered by Sezer et al. (2011) using the assumption of full-ionisation equilibrium to calculate a plasma age of $\sim 3 \times 10^4 \sqrt{f}$, where f is the plasma filling-factor within a spherical region. With the benefit of the latest distance analyses by TL2012, this estimate may be scaled upwards by ~ 20 -80%, to account for a nearer distance to CTB 37A (6.3-9.5 kpc).

To complement the work of Sezer et al. (2011), similarities of CTB 37A with other SNRs cannot be overlooked. Referring to Green et al. (1997), which summarises SNRs with detected associated OH maser emission, and cross-checking these with SNR catalogues (Guseinov et al. 2003, 2004a,b), a short list of OH maser-associated SNRs with estimated ages can be compiled: W28 ($\sim 10^4$ yr), W44 ($\sim 10^4$ yr), W51c ($\sim 10^4$ yr), IC 443 ($\sim 10^3$ yr), CTB 33 ($\leq 10^5$ yr) and G347+0.2 ($\sim 10^3$ yr). Of these, the first 4 SNRs have diameters of ~ 15 -35 pc, similar to CTB 37A which has dimensions of $\sim 0.12^\circ \times 0.23^\circ$ and an average diameter of $\sim 24 \pm 5$ pc at a distance of 7.9 ± 1.6 . Based purely on these similarities, the CTB 37A age may be of the order of 10^3 - 10^4 yr.

Further support for a $\sim 10^3$ - 10^4 yr age for CTB 37A comes from assuming a standard Sedov-Taylor time-scaling of the shock-radius (here taken from Caprioli et al. (2009), Equation 29). For an ejecta with energy 10^{51} erg expanding into a medium of number density 10 cm⁻³, similar to towards HESS J1714-385 (although the shock radius is only weakly dependent on density, being proportional to $n^{-1/5}$), the shock radius reaches $\sim 24 \pm 5$ pc after $\sim 0.6_{-0.3}^{+0.4} \times 10^4$ yr. Certainly, the old age is consistent with the large fraction of energy possibly injected into the $v_{LSR} \sim -60$ km s⁻¹ cloud by CTB 37A (4-40%, § 5.2), assuming an ejecta energy of 10^{51} erg.

Finally, Aharonian et al. (1996) model the diffusion of CRs away from a continuous accelerator and plot the energy-dependent CR-enhancement factor for different SNR ages.

We assume that slow CR diffusion, like that seen towards the similar SNR, W28 (see eg. Aharonian et al., 2008b and Gabici et al., 2010), applies to the CTB 37A region. On referring to Figure 2b in Aharonian et al. (1996), which corresponds to a galactic CR diffusion coefficient (parameterised from a CR energy of 10 GeV) of 10^{26} cm²s⁻¹ and a source CR spectrum of spectral index $\gamma = -2.2$, a CR-enhancement of ~ 80 -300 at TeV energies corresponds to an age of 10^4 - 10^5 yr (at a distance of 10 pc from the CR release point). The range of the models considered by Aharonian et al. (1996) does not suggest CR enhancement factors above ~ 300 . We note that the CR enhancement factor resulting from a normal (in contrast to ‘slow’) galactic diffusion coefficient of 10^{28} cm²s⁻¹ is substantially lower (2-3 \times the local value), inconsistent with the calculated CR enhancement range, but we favour the W28-region CR diffusion speed due to the physical similarities with CTB 37A (see above).

The range of age values suggested by this CR enhancement argument (10^4 - 10^5 yr) spans larger values than those suggested by the previous 3 methods (the plasma age, comparison with similar remnants and the Sedov-Taylor scaling relation). If a leptonic component of gamma-ray emission was present, CR enhancement would be less than that calculated here. It also follows that the age would be overestimated by our CR enhancement factor argument.

Through this CR-enhancement factor argument, the simplistic shock-radius model, and the aforementioned similarities to other SNRs, we find that the age of CTB 37A is consistent with the previous result of Sezer et al. (2011) (for $f \sim 1$), of the order $\sim 10^4$ yr.

6 CONCLUSIONS

Using CO(2-1), CS(1-0) and HI spectra, we conducted an investigation of the atomic and molecular gas towards the CTB 37A region, which has signatures of a shock-gas interaction (OH masers, thermal X-rays) and is a source of TeV gamma rays, possibly hadronic in origin.

CS(1-0) observations identified new dense gas components associated with 4 of the 6 observed locations that exhibit 1720 MHz OH maser emission.

CO(2-1), CS(1-0) and HI emission, and HI absorption allowed the estimation of lower limits of column density towards regions of interest. Column density lower limits to-

wards X-ray emission regions are consistent with X-ray absorption measurement-derived column densities.

CO(2-1), CS(1-0) and HI-derived mass estimates for specific gas components towards the CTB 37A region allowed an investigation of the CR hadron-target mass available. Assuming that all measured mass (and an assumed additional 25% He mass) in the HESS gamma-ray emission region is potential CR target material in a hadronic scenario for TeV gamma-ray emission, we estimate a CR density of $\sim 80-1100\times$ that seen at Earth.

Based on a comparison of CTB 37A to other SNRs associated with OH-maser emission, Sedov-Taylor phase scaling of the CTB 37A shock radius, and an examination of the expected change in CR-enhancement factor with time, we estimate the CTB 37A age to be consistent with previous estimates of $\sim 10^4$ yr.

High resolution ($\sim 1'$), high energy (GeV-TeV) measurements, such as what may be expected from future ground-based gamma-ray telescopes (The CTA Consortium 2011), would allow a more detailed investigation of the nature of the high energy spectrum towards CTB 37A, especially with regard to the spatial correspondence with molecular gas.

7 ACKNOWLEDGMENTS

This work was supported by an Australian Research Council grant (DP0662810, 1096533). The Mopra Telescope is part of the Australia Telescope and is funded by the Commonwealth of Australia for operation as a National Facility managed by the CSIRO. The University of New South Wales Mopra Spectrometer Digital Filter Bank used for these Mopra observations was provided with support from the Australian Research Council, together with the University of New South Wales, University of Sydney, Monash University and the CSIRO.

We thank Naomi McClure-Griffiths for feedback regarding our HI analysis and our anonymous referee for his/her detailed constructive criticism of our manuscript.

REFERENCES

- Aharonian F., 1991, *Ap&SS*, 180, 305A-320A
 Aharonian F., 1991, *A&A*, 309, 917-928
 Aharonian F. et al.(HESS Collab.), 2007, *A&A*, 464, 235-243
 Aharonian F. et al.(HESS Collab.), 2008, *A&A*, 490, 685
 Aharonian F. et al.(HESS Collab.), 2008, *A&A*, 481, 401-410
 Arikawa Y., Tatematsu K., Sekimoto Y. & Takahashi T., 1999 *Publ. Astron. Soc. Japan* 51, L7-L10
 Bohlin R. C., Savage B. D. & Drake J. F., 1978, *ApJ*, 224, 132
 Brand J. & Blitz L., 1993, *A&A*, 275, 67-90
 Brandt T. J., (Fermi-LAT Collab.), 2011, A view of supernova remnant CTB 37A with the Fermi Gamma-ray Telescope. *J. Adv. Space Res.*, doi:10.1016/j.asr.2011.07.021
 Brogan C., Frail D., Goss W. & Troland T., 2000, *ApJ*, 537, 875-890
 Caprioli D., Blasi P. & Amato E, 2009, *MNRAS*, 396, 2065-2073
 Casanova S., 2011, *PrPNP*, 66, 681-685
 Castro D. & Slane P., 2010, *ApJ*, 717, 372-378
 Caswell J., Murray J., Roger R., Cole D. & Cooke D., 1975, *A&A*, 45, 239-258
 Churchwell E. et al., 2006, *ApJ*, 649, 759-778
 Clark D., Green A. & Caswell J., *AuJPA*, 1975, 37, 75C
 The CTA Consortium, 2011, arXiv:1111.2183
 Dame T., Hartmann D. & Thaddeus P., 2001, *ApJ*, 547, 792-813
 Dickey J. M. & Lockman F. J., 1990, *ARA&A*, 28, 215-261
 Draine B., Roberge W. & Dalgarno A., 1983, *ApJ*, 264, 485-507
 Feinstein F., Fiasson A., Gallant Y., Chaves R., Marandon V., de Naurious M., Kosack K. & Rowell G., 2009, *AIPC*, 1112, 54P
 Frail D., Goss W., Reynoso E., Giacani E., Green A. & Otrupcek R., 1996, 111, 1651-59
 Frail D. & Mitchell G., 1998, 508, 690-695
 Frerking M., Wilson R., Linke R. & Wannier P., 1980, *ApJ*, 240, 65-73
 Fukui Y., Sano H., Sato J., Horachi H., Torii K., McClure-Griffiths N., Rowell G., Aharonian F. et al., 2012, *ApJ*, 746, 82
 Gabici S., Aharonian F. & Casanova S., 2009, *MNRAS*, 396, 1629-1639
 Gabici S., Casanova S., Aharonian F. & Rowell G., 2010, in Boissier S., Heydari-Malayeri M., Samadi R., Valls-Gaband D., eds, *Proc. French Soc. Astron. Astrophys.*, SF2A, 313-317
 Goldsmith P. & Langer W., 1999, *ApJ*, 517, 209-225
 Green A., Frail D., Goss W. & Otrupcek R. 1997, *AJ*, 114, 2058-2067
 Green A. et al., 1999, *ApJS*, 122, 207
 Guseinov O., Ankey A. & Tagieva S., 2003, *Serb. Astron. J.*, 167, 93-110
 Guseinov O., Ankey A. & Tagieva S., 2004, *Serb. Astron. J.*, 168, 55-69
 Guseinov O., Ankey A. & Tagieva S., 2004, *Serb. Astron. J.*, 168, 65-82
 Hartman R. et al., 1999, *ApJS*, 123, 79
 Haverkorn M., Gaensler B. M., McClure-Griffiths N. M., Dickey J. M. & Green A. J., 2006, *ApJS*, 167, 230
 Hewitt J., Yusef-Zadeh F. & Wardle M., 2008, *ApJ*, 683, 189-206
 Kassim N., Baum S. & Weiler K., 1991, *ApJ*, 374, 212-217
 Kerr F. & Lynden-Bell D., 1986, *MNRAS*, 221, 1023-1038
 Liszt H S. & Lucas R., 2002, *A&A*, 391, 693
 Liszt H S., Pety J. & Lucas R., 2010, *A&A*, 518, A45
 Maxted N., Rowell G., Dawson B., Burton M., Nicholas B., Fukui Y., Walsh A., Kawamura A., Horachi H. & Sano H., 2012, *MNRAS*, 419, 251-266
 McClure-Griffiths N., Dickey J., Gaensler B., Green A., Haverkorn M. & Strasser S., 2005, *ApJ*, 158, 178-187
 Milne D., Goss W., Haynes R., Wellington K., Caswell J. & Skellern D., 1979, *MNRAS*, 188, 437-444
 Moriguchi Y, Tamura K, Tawara Y, Sasago H, Yamaoka T, Onishi T & Fukui Y, 2005, *ApJ*, 631, 947-963
 Nicholas B., Rowell G., Burton M., Walsh A., Fukui Y., Kawamura A., Longmore S. & Keto E. 2011, *MNRAS*, 411, 1367-1385
 Nicholas B., Rowell G., Burton M., Walsh A., Fukui Y., Kawamura A. & Maxted, N., 2012, *MNRAS*, 419, 251-

266

- Protheroe R., Ott J., Ekers R., Jones D. & Crocker R., 2008, MNRAS, 390, 683-692
- Reach W., Rho J., Tappe A., Pannuti T., Brogan C., et al. 2006, ApJ, 131, 1479-1500
- Reynoso E. & Mangum J., 2000, ApJ, 545, 874-884
- Sezer A., Gok F., Hudaverdi M. & Ercan E., 2011, MNRAS, 417, 1387-1391
- Slane P., Gaensler B., Dame T., Hughes J., Plucinsky P. & Green A., 1999, 525, 357-367
- Tian W. & Leahy D., 2012, MNRAS, 421, 2593-2597
- Urquhart J., Hoare M., Purcell C., Brooks K., Voronkov M., Indermuehle B., Burton M., Tothill N. & Edwards P., 2010, PASA, 27, 321-330
- Vallee J., 2005, ApJ, 130, 569-575
- Vallee J., 2008, ApJ, 135, 1301-1310
- van Dishoeck E. & Blake G., 1998, ARA&A, 36, 317-368
- Walsh A., Lo N., Burton M., White G., Purcell C., Longmore S., Phillips C. & Brooks K., 2008, PASA, 25, 105.
- Wolfire M., Hollenbach D. & McKee C., 2010, 716, 1191-1207.

APPENDIX A: INFRARED EMISSION TOWARDS CTB 37A

Evidence for shock-interactions are also seen at infrared wavelengths. Reynoso & Mangum (2000) noted the presence of shocked, heated dust, IRAS 17111–3824, towards a region of overlap between CTB 37A and G348.5–0.0. Reach et al. (2006) later discovered several patches and filaments of $4.5\ \mu\text{m}$ emission towards and around Locations 5 and 6, possibly indicating shocked H_2 gas. The authors also note further evidence for shocked gas at $5.8\text{--}8\ \mu\text{m}$ towards the CTB 37A-G348.5–0.0 overlap region.

Figure A1 is an image of 24, 8 and $5.8\ \mu\text{m}$ infrared emission. Millimetre star-formation indicators (HC_3N , CH_3OH , SiO , Figure B2) are seen towards Location 3 ($v_{\text{LSR}} \sim -110\ \text{km s}^{-1}$), but no clear association is seen at infrared wavelengths. Faint $8\ \mu\text{m}$ emission may indicate warm dust, but this extends over a large region of the centre of CTB 37A and is most intense in the region surrounding Location 4. This characteristic, however, does not rule out the notion that warm dust may be responsible for the millimetre molecular emission towards Location 3.

North of Location 3, a shell of $8\ \mu\text{m}$ emission $0.02\text{--}0.03^\circ$ in diameter, can be seen surrounding a compact $24\ \mu\text{m}$ source. This is likely to be a wind-blown bubble surrounding a high-mass O or B star (object S5 from Churchwell et al., 2006), unrelated to CTB 37A and HESS J1714–385.

Emission at $24\ \mu\text{m}$ surrounding $(l,b) \sim (348.37, 0.14)$ clearly shows hot dust obscured by a infrared-dark absorber, likely a cold foreground cloud. $\text{CO}(2-1)$ emission at $v_{\text{LSR}} \sim -10\ \text{km s}^{-1}$ is observed towards this region, but the CO-traced gas is too uniform across CTB 37A's north-west to explain the localised 'finger' of infrared-absorption. Observations of the cold, dense gas tracer $\text{NH}_3(1,1)$ were employed in an attempt to aid in constraining the absorber's location, but we found no $\text{NH}_3(1,1)$ emission towards this location in the low-exposure HOPS galactic plane data (Walsh et al. 2008) and a follow-up high-exposure ($T_{\text{RMS}} \sim 0.1\ \text{K ch}^{-1}$) deep pointing revealed no $\text{NH}_3(1,1)$ emission either.

APPENDIX B: ADDITIONAL 7 MM IMAGES TOWARDS CTB 37A

Figure B1 is a position-velocity image towards the CTB 37A region. Similar to Figure 2, several clouds are visible in $\text{CO}(2-1)$ at approximate line-of-sight reference velocities, $v_{\text{LSR}} \sim -10, -20, -60$ to $-75, -90$ and $-105\ \text{km s}^{-1}$. Corresponding $\text{CS}(1-0)$ emission is observed towards $\text{CO}(2-1)$ -traced clouds at approximate line-of-sight reference velocities, $v_{\text{LSR}} \sim -10, -60$ to $-75, -90$ and $-105\ \text{km s}^{-1}$, indicating dense gas at these locations.

Figure B2a/b/c are three images of emission from the HC_3N , CH_3OH and SiO molecules. The narrow spectral line profile and correspondence with a molecular core seen in $\text{CO}(2-1)$ and $\text{CS}(1-0)$ emission, suggest possible star-formation activity.

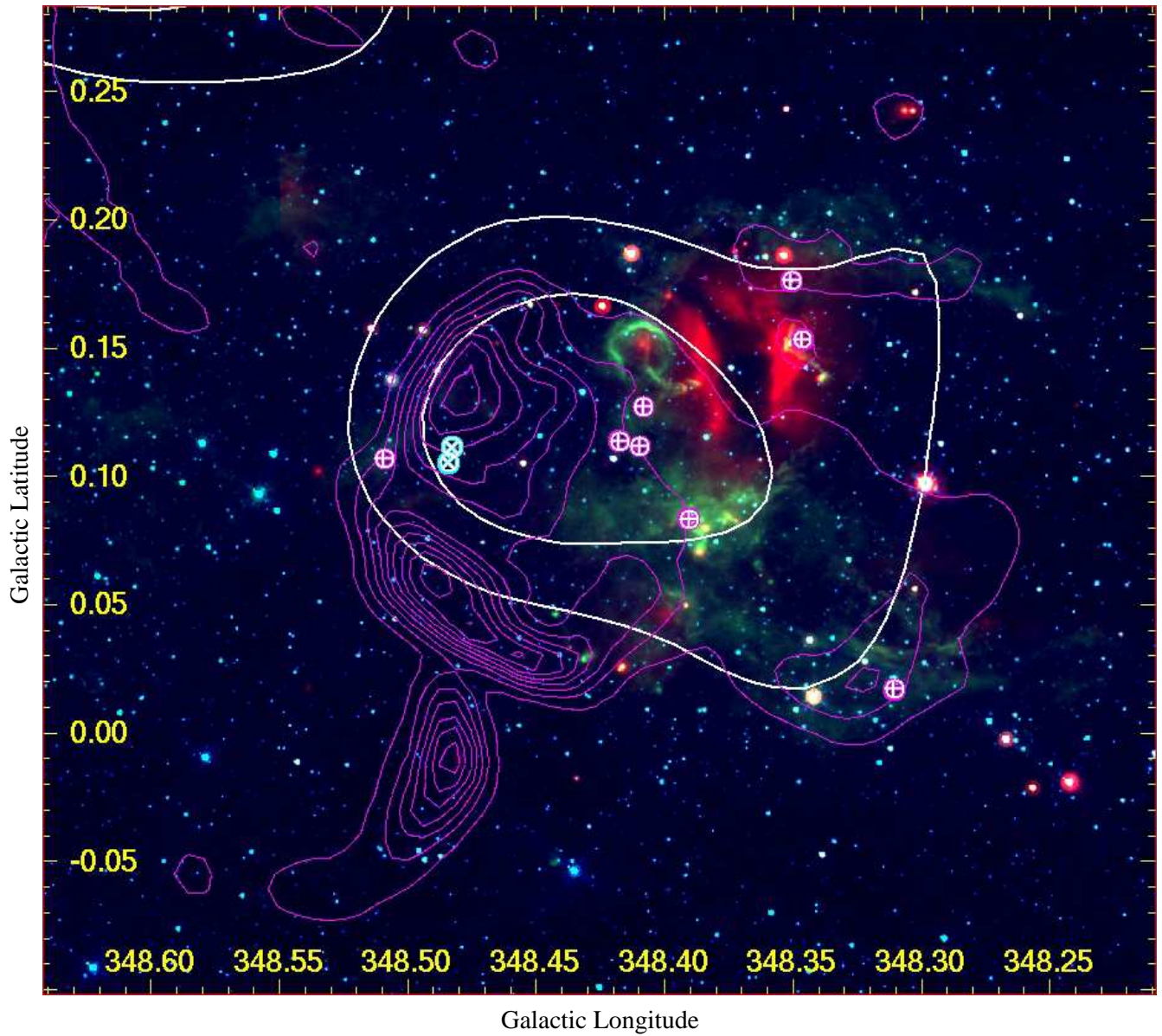


Figure A1. Spitzer $24\ \mu\text{m}$, $8\ \mu\text{m}$ and $5.8\ \mu\text{m}$ emission are shown in red, green and blue, respectively. White contours show HESS 80 and 100 excess count gamma-ray emission, and magenta contours show Molonglo 843 MHz radio continuum emission. Crosses represent both the $\sim -65\ \text{km s}^{-1}$ (pink, +) and $\sim -25\ \text{km s}^{-1}$ (cyan, \times) OH maser populations (Frail et al. 1996).

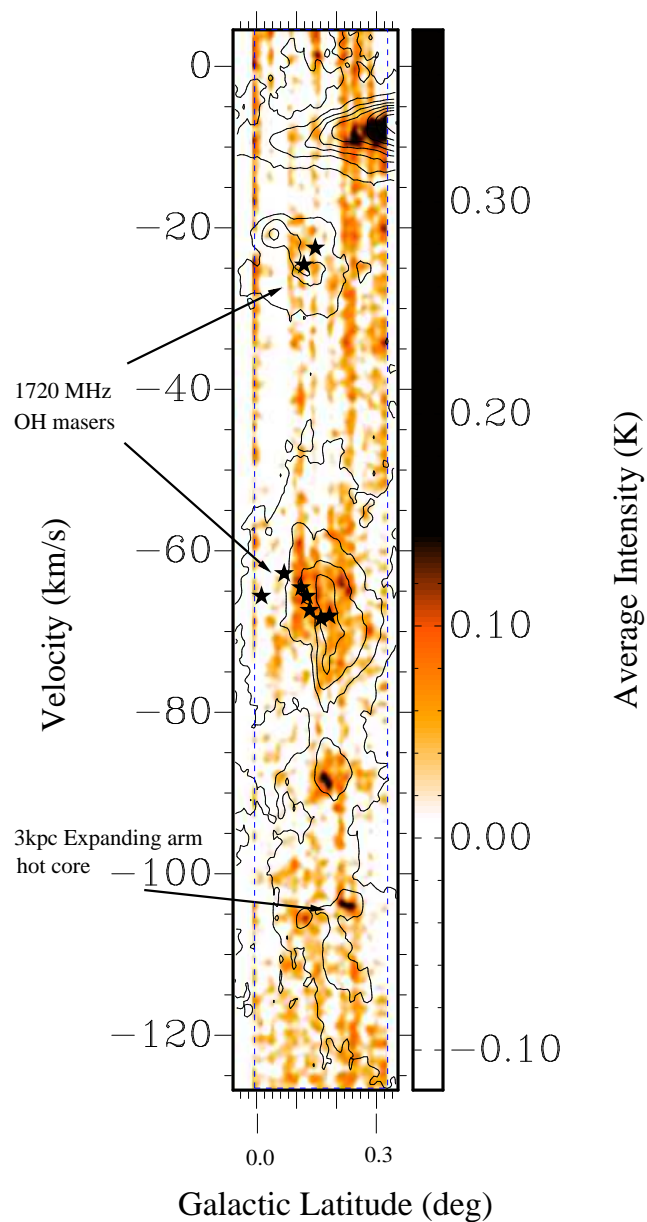


Figure B1. Position-velocity image of Mopra CS(1-0) emission towards the CTB 37A region. Nanten CO(2-1) emission contours towards the CTB 37A region are overlaid. Black stars indicate 1720 MHz OH maser locations and the dashed lines indicate the extent of the 7 mm mapping campaign for CS(1-0) emission.

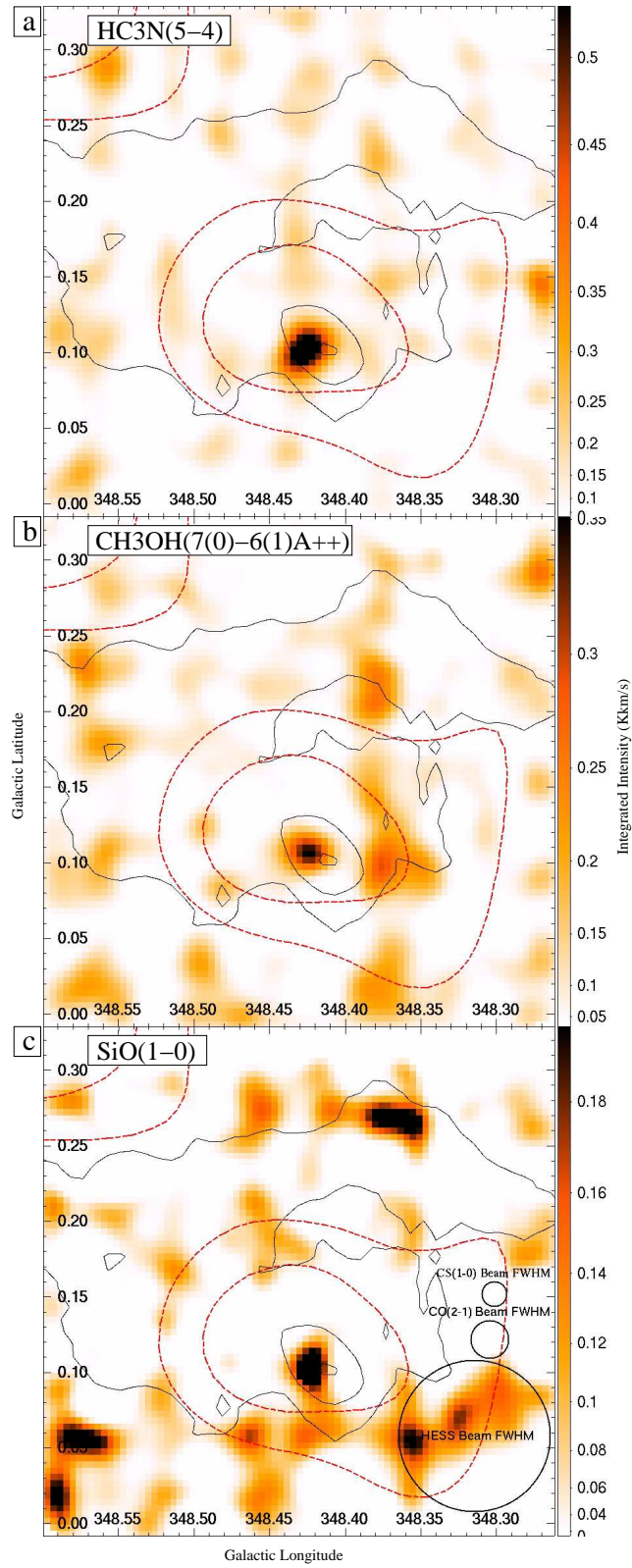


Figure B2. Various spectral line emissions integrated between $v_{\text{LSR}} = -108$ and -102 km s^{-1} . Black contours indicate CO(2-1) integrated intensity levels of 10, 20 and 30 K km s^{-1} and red dashed contours indicate HESS 80 and 100 excess count gamma-ray emission. See § 4.5 for details.